



Correction of spatially varying stratified atmospheric delays in multitemporal InSAR

Hongyu Liang^a, Lei Zhang^{a,*}, Zhong Lu^b, Xin Li^c

^a College of Surveying and Geo-Informatics, Tongji University, Shanghai 200092, China

^b Roy M. Huffington Department of Earth Sciences, South Methodist University, Dallas, TX 75275, USA

^c Institute of Geographic Sciences and Natural Resources Research, Chinese Academy of Sciences, Beijing 100101, China

ARTICLE INFO

Edited by Jing M. Chen

Keywords:

Multitemporal InSAR

Tropospheric delay

Joint model

Elevation-correlated deformation

ABSTRACT

Tropospheric delay is a major limiting factor in ground displacement retrieval using interferometric synthetic aperture radar (InSAR). Such delays are caused by the variations of pressure, temperature, and humidity of the troposphere, potentially leading to elevation-dependent phases in interferograms. The atmospheric heterogeneity makes the phase-elevation dependence vary in both space and time, posing challenges on empirical models that estimated the elevation-topography relationship in empirically predefined windows interferogram by interferogram. Moreover, the portion of the deformation that is correlated with topography can be mistaken as tropospheric delays and therefore degrade the performance of linear regression between the tropospheric phase and the elevation. The effectiveness of these methods is further limited by the requisite knowledge presumed of the user, particularly with regard to how to divide the scene and which observation model is suitable. These limitations make reliable isolation of tropospheric delay challenging. We present here a novel approach that combines tropospheric delay, deformation and possible topographic error to a joint model, enabling a precise separation of tropospheric delay. The rationale is rooted in the distinct temporal dependencies of these parameters. To avoid empirical setting of segmentation windows, we employ quadtree to adaptively control the spatial variability of tropospheric properties. We validate the proposed method at two volcanic areas, Bali and Hawaii, where tropospheric delay presents notable variability coupled with elevation-correlated deformation signals. Both ascending and descending Sentinel-1 data over the island of Bali show that the proposed method outperforms the conventional ones. The misfit standard deviation (STD) is reduced by ~50% at the island of Bali, where elevation-correlated deformation is simulated according to a predefined model. More impressively, at the island of Hawaii, the misfit STD between InSAR and ground truth (i.e., GPS displacements) decreases from 25.1 to 4.5 mm. The experimental results demonstrate that the proposed method is effective in reducing the spatially variable tropospheric delay while preserving the elevation-correlated deformation signal.

1. Introduction

Interferometric synthetic aperture radar (InSAR) nowadays has proven to be a powerful technique for mapping ground deformation caused by natural or anthropogenic activities (Lu and Dzurisin, 2014; Massonnet et al., 1993; Wu et al., 2020; Zhang et al., 2012). The accurate retrieval of deformation signal from InSAR measurements is primarily limited by tropospheric delay, which could lead to deformation error of tens of centimeters (Ding et al., 2008; Zebker et al., 1997). The tropospheric delay within interferogram represents the difference of atmospheric delays between two SAR acquisitions, which mainly arise from

the variations of temperature, pressure and humidity in neutral troposphere. From the point of physical origin, the tropospheric delay is split into two terms, i.e., hydrostatic and wet delays (Berrada Baby et al., 1988; Bevis et al., 1992). The hydrostatic delay that is related to the distribution of pressure and temperature varies smoothly in both space and time, leading to a compound of topography-dependent and lateral phase variations. The wet delay occurs with the rapid variations of water vapor and temperature in a small-scale dimension, resulting in an irregular phase distribution (Hanssen, 2001; Markowski and Richardson, 2011). This study aims to solve the spatially varying tropospheric delays in multitemporal InSAR (MTInSAR) observations for large-scale

* Corresponding author.

E-mail address: lszhang@tongji.edu.cn (L. Zhang).

area.

In the past decades, various tropospheric delay correction approaches have been proposed and can be generally classified into two categories, i.e., external data based and interferometric phase based. The more straightforward correction approach utilizes external auxiliary datasets including weather reanalysis products or operational forecasting models (Doin et al., 2009; Jolivet et al., 2014), Global Positioning System (GPS) zenith total delay (ZTD) (Onn and Zebker, 2006; Yu et al., 2018), and multi-spectral data (Li et al., 2005), etc. These external data based approaches have been implemented with variable degrees of success, however, they are inherently limited by the auxiliary data's precision as well as spatial and temporal resolutions. For example, the GPS-based correction can only work in the vicinity of individual GPS sites; the spectrometers are restricted by cloud-free and daylight conditions; and the weather models require spatiotemporal interpolation to match the interferograms, potentially introducing large uncertainties. The integration of two or more independent data is theoretically more robust than a single dataset, but its performance still largely depends on the precision and distribution of the auxiliary measurement(s) (Li et al., 2005; Yu et al., 2018).

The second approach, interferometric phase based correction, benefits from the development of advanced MTInSAR techniques, such as Persistent Scatterer Interferometry (PSI) (Ferretti et al., 2001; Hooper et al., 2007; Werner et al., 2003) and Small Baseline Subset (SBAS) (Berardino et al., 2002). The phase variations are considered to be temporally independent and correlated in space to some extent. Accordingly, the MTInSAR approaches mitigate the undesired phases by adopting spatiotemporal filtering or iterative filtering process (Crosetto et al., 2002; Wegmuller et al., 2010). However, the determination of the filtering window size is subjective due to the fact that tropospheric delay is not Gaussian-distributed in temporal domain (Cao et al., 2017).

An alternative phase-based correction approach involves using the relationship between the interferometric phase and the elevation (Bekaert et al., 2015; Liang et al., 2019). Since the hydrostatic delay in the troposphere is path-dependent, the interferometric phase induced by the delay has a strong correlation with elevation, especially in regions with high relief. The scenario applies to ground-based InSAR observations, where tropospheric delay shows strong correlation with two terms of radar-to-target distance and elevation, respectively (Deng et al., 2022; Iglesias et al., 2014; Pipia et al., 2008). Currently, several approaches have been developed to describe the relationship based on either linear or power-law functions in deformation-free areas (Bekaert et al., 2015; Falabella et al., 2022; Murray et al., 2020). However, there are several limitations associated with current methods on correcting the elevation-dependent phase. The first limitation in the current methods is that window segmentation is mainly conducted empirically in terms of window size and quantity (Bekaert et al., 2015; Deng et al., 2022; Murray et al., 2020). The second shortcoming is about neglecting the coupling effect between deformation and topography. When the deformation has a relationship with topography (e.g., deformation at volcanic mountains), the elevation-correlated deformation will be mistaken as tropospheric delay in the current model, degrading the accuracy of the deformation retrieval.

In this study, we propose an improved tropospheric correction method to tackle the aforementioned issues. We firstly explore a window segmentation strategy that can adaptively divide the study area based on the statistics of phase variations. In each local window, we parameterize the elevation-dependent and lateral tropospheric delay in a trilinear form. We then develop a joint model to simultaneously estimate tropospheric delay, deformation, and possible topographic error. Since the tropospheric delay is usually considered to be temporally independent while the deformation is correlated with time, when the two parameters are modelled, they can be separated according to their distinct temporal behaviors. We apply the new method at the islands of Bali and Hawaii where the signals of volcanic unrest and tropospheric delay are usually mixed within interferograms. The performance for tropospheric

mitigation is validated by considering both phase standard deviation and agreement with simulated and GPS-measured displacements.

2. Methodology

2.1. Tropospheric delay modelling

Let us start with m multi-reference interferograms generated from $n + 1$ SAR images. After subtracting topographic phase components by using external digital elevation model (DEM) (e.g., SRTM DEM), the interferograms are unwrapped with respect to a common reference point. In order to mitigate the spatial variability of troposphere, the unwrapped interferograms are divided into a set of small windows with overlapping area by quadtree segmentation (Section 2.4). For an interferogram composed by SAR images i and j , the unwrapped phase within a local window can be represented by the sum of multiple phase contributions,

$$\varphi_{total}^{ij} = (\varphi_{trop}^i - \varphi_{trop}^j) + \varphi_{defo}^{ij} + \varphi_{topo}^{ij} + \varphi_{other}^{ij} \quad (1)$$

where φ_{trop}^i and φ_{trop}^j represent the vectors of tropospheric delays in SAR images i and j , respectively. φ_{defo}^{ij} is the unwrapped phase vector due to deformation between SAR acquisitions i and j , φ_{topo}^{ij} denotes the phase residual vector due to inaccurate external DEM, and φ_{other}^{ij} refers to the vector of remaining phase components including unmodelled deformation, turbulent delay, and decorrelation noise. Given that the tropospheric delay phase in an interferogram represents the difference of delay phases between two SAR acquisitions, we can parameterize the delay parameters in each SAR acquisition by.

$$\varphi_{trop}^i = a^i \bullet X + b^i \bullet Y + c^i \bullet X \bullet Y + d^i \bullet H + \varphi_0^i \quad (2)$$

Where i is the index of SAR image, a^i, b^i, c^i, d^i and φ_0^i are the unknown coefficients to be estimated; X and Y are the vectors of spatial coordinates in range direction and azimuth direction, respectively; H is the elevation. The $X \bullet Y$ term that jointly modulates the range and azimuth directions is used to account for nonlinear phase trend, while the inclusion of this term is optional depending on phase variation complexity. If the local window contains s coherent points, Eq. (2) can be reformed as

$$\varphi_{trop}^i = A \bullet P_{trop}^i \quad (3)$$

with

$$A = [X, Y, XY, H, 1]$$

$$P_{trop}^i = [a^i, b^i, c^i, d^i, \varphi_0^i]^T \quad (4)$$

where A is an $s \times 5$ design matrix, P_{trop}^i is a 5×1 vector of unknown coefficients at each SAR acquisition. Since the interferometric phase reflects the difference of signals that are strictly closed in temporal loop (e.g., atmospheric, topographic and geophysical signals), the tropospheric delays in m interferograms can be linearly expressed as the combination of those of $n + 1$ SAR images (Biggs et al., 2007; Zhang et al., 2014),

$$\Phi_{trop} = B_{trop} \bullet P_{trop} \quad (5)$$

with

$$B_{trop} = A \otimes F$$

$$P_{trop} = [P_{trop}^1, P_{trop}^2, \dots, P_{trop}^n]^T \quad (6)$$

where \otimes represents the Kronecker tensor product, B_{trop} is an $(s \times m) \times (5 \times n)$ design matrix, P_{trop} represents a $(5 \times n) \times 1$ vector of unknown coefficients of n SAR images with respect to a reference SAR acquisition.

\mathbf{F} is an $m \times n$ transfer matrix from SAR image to interferometric pair, which has the form of

$$\mathbf{F} = \begin{bmatrix} 1 & 0 & -1 & \cdots & 0 \\ 0 & 1 & \cdots & -1 & 0 \\ \vdots & \vdots & \vdots & \vdots & \vdots \\ 0 & 0 & 1 & 0 & -1 \end{bmatrix}_{m \times n} \quad (7)$$

where 1 and -1 represent the primary and secondary SAR images in an interferometric pair, respectively. For simplicity without the loss of generality, we assume tropospheric delay coefficients in the reference image are zeros. The column corresponding to the reference SAR image has been deleted.

2.2. Deformation and topographic error modelling

As mentioned previously, the tropospheric phase-elevation dependence can be biased by deformation and topographic error, especially when the deformation signal is correlated with elevation. Considering the deformation and the tropospheric delay have distinct temporal dependencies, we model the temporal low-pass (LP) component of deformation signal jointly with the tropospheric delay and the topographic error. The cubic polynomial is employed to characterize the temporal behavior of displacement. For a given pixel p in an interferogram within a local window, the sum of the deformation and the topographic error is expressed as

$$\phi_{defo+topo,p}^{i,j} = \frac{4\pi}{\lambda} \cdot \left[\bar{v}_p(t_j - t_i) + \frac{1}{2}\bar{a}_p(t_j - t_i)^2 + \frac{1}{6}\bar{\Delta a}_p(t_j - t_i)^3 \right] + \frac{4\pi}{\lambda} \cdot \frac{B_{\perp}^{i,j} \Delta h_p}{r \sin \theta} \quad (8)$$

where \bar{v}_p , \bar{a}_p , and $\bar{\Delta a}_p$ are three unknown parameters related to the mean velocity, the mean acceleration, and the mean acceleration variation, respectively. λ is the radar wavelength, r is the slant range distance between SAR sensor and ground surface, θ is the look angle, $B_{\perp}^{i,j}$ is the perpendicular baseline of the interferogram, and Δh_p denotes the topographic error. Note Eq. (8) can be easily extended to include seasonal, Heaviside, and exponential/logarithmic terms to represent the deformation associated with groundwater, cos-seismic/co-eruptive, and post-seismic/post-eruptive processes, respectively (Agram et al., 2013). Considering m interferometric pairs, Eq. (8) can be reformed as

$$\phi_{defo+topo,p} = [\mathbf{G} \bullet \mathbf{D}_{defo}, \mathbf{D}_{topo}] \bullet \mathbf{P}_{defo+topo,p} \quad (9)$$

with

$$\mathbf{D}_{defo} = \frac{4\pi}{\lambda} \cdot \begin{bmatrix} 1 & \frac{t_1 - t_0}{2} & \frac{(t_1 - t_0)^2}{6} \\ 1 & \frac{t_2 - t_1 - 2t_0}{2} & \frac{(t_2 - t_1)^3 - (t_1 - t_0)^3}{6(t_2 - t_1)} \\ \cdots & \cdots & \cdots \\ 1 & \frac{t_n + t_{n-1} - 2t_0}{2} & \frac{(t_n - t_0)^3 - (t_{n-1} - t_0)^3}{6(t_n - t_{n-1})} \end{bmatrix}_{n \times 3}$$

$$\mathbf{D}_{topo} = \left[\frac{4\pi}{\lambda} \cdot \frac{B_{\perp}^1}{r \sin \theta}, \frac{4\pi}{\lambda} \cdot \frac{B_{\perp}^2}{r \sin \theta}, \cdots, \frac{4\pi}{\lambda} \cdot \frac{B_{\perp}^m}{r \sin \theta} \right]^T$$

$$\mathbf{P}_{defo+topo,p} = [\bar{v}_p, \bar{a}_p, \bar{\Delta a}_p, \Delta h_p]^T \quad (10)$$

where \mathbf{G} is an $m \times n$ transfer matrix. The generic element $G(k, l)$ can be determined as: if the k th interferogram is constructed by SAR images i and j ($i < j$), then $G(k, l) = t_{j+1} - t_i$ for $i \leq l \leq j$, and $G(k, l) = 0$ elsewhere. t_l represents the acquisition date of the l th SAR image. \mathbf{D}_{topo} is an $m \times 1$ vector that is related to the coefficient of topographic error. $\mathbf{P}_{defo+topo,p}$ is

a 4×1 vector of unknown parameters related to the deformation and the topographic error. Considering s pixels are available for estimation, the phase contributions due to the temporal LP deformation and the topographic error in m interferograms are expressed as

$$\Phi_{defo+topo} = \mathbf{B}_{defo+topo} \bullet \mathbf{P}_{defo+topo} \quad (11)$$

with

$$\mathbf{B}_{defo+topo} = [\mathbf{G} \bullet \mathbf{D}_{defo}, \mathbf{D}_{topo}] \otimes \mathbf{I}_{s \times s}$$

$$\mathbf{P}_{defo+topo} = [P_{defo+topo,1}, P_{defo+topo,2}, \cdots, P_{defo+topo,s}]^T \quad (12)$$

where $\mathbf{B}_{defo+topo}$ is an $(s \times m) \times (4 \times s)$ design matrix, $\mathbf{P}_{defo+topo}$ represents a $(4 \times s) \times 1$ vector including unknown parameters of the deformation and the topographic error for s points. $\mathbf{I}_{s \times s}$ is an $s \times s$ identity matrix.

2.3. Parameter estimation

In order to simultaneously estimate the tropospheric delay, the deformation and the topographic error, we combine Eq. (5) and Eq. (11) to a joint model. Therefore, the relationship between the unwrapped phase observations and the modelled phase contributions in m interferograms and s points can be expressed as

$$\Phi = \mathbf{B} \bullet \mathbf{P} + \mathbf{R} \quad (13)$$

with

$$\mathbf{B} = [\mathbf{B}_{defo+topo}, \mathbf{B}_{trop}]$$

$$\mathbf{P} = [P_{defo+topo}^T, P_{trop}^T]^T \quad (14)$$

where \mathbf{R} is a $(5 \times n + 4 \times s) \times 1$ residual vector that contains the sum of unmodelled deformation, turbulence, decorrelation noise. Because Eq. (13) is a large sparse linear system, sparse matrix factorization is a better choice than ordinary least squares (LS) to solve the equation (Zhang et al., 2014). In this study, we employ Golub-Kahan bidiagonalization with L2-norm minimization to iteratively derive the optimal solution (Fong and Saunders, 2011). Once the unknown parameters are obtained, the tropospheric delay within the local window for each SAR acquisition is derived by using (2) and (3). The corrected interferogram phase in each local window is obtained by

$$\phi_{trop,corr}^{i,j} = \phi_{total}^{i,j} - (\phi_{trop}^j - \phi_{trop}^i) \quad (15)$$

Note that after correcting the tropospheric delay in each local window, the spatial variability of troposphere might cause phase discontinuities between adjacent windows. To tackle this, we adopt Delaunay triangulation to convert the point phases into the phase differences of arcs. In the overlapping areas, the phase differences of common arcs might be slightly different because of independent estimation in each local window. The inconsistent phase differences can be smoothed by using average values. Then, the corrected phases at points and the phase differences at arcs are linked by

$$\Delta \phi_{trop,corr}^{i,j} = \mathbf{C} \bullet \tilde{\phi}_{trop,corr}^{i,j} \quad (16)$$

where $\tilde{\phi}_{trop,corr}^{i,j}$ represents a vector of corrected phases at points, and $\Delta \phi_{trop,corr}^{i,j}$ represents a vector of corrected phase differences at arcs. \mathbf{C} is transfer matrix relating point to arc in the whole interferogram, which is composed of 1, -1 and 0 elements. Note that the column relative to the reference point in \mathbf{C} has been deleted to avoid rank deficiency. The corrected phases $\tilde{\phi}_{trop,corr}^{i,j}$ can be derived by sparse least squares.

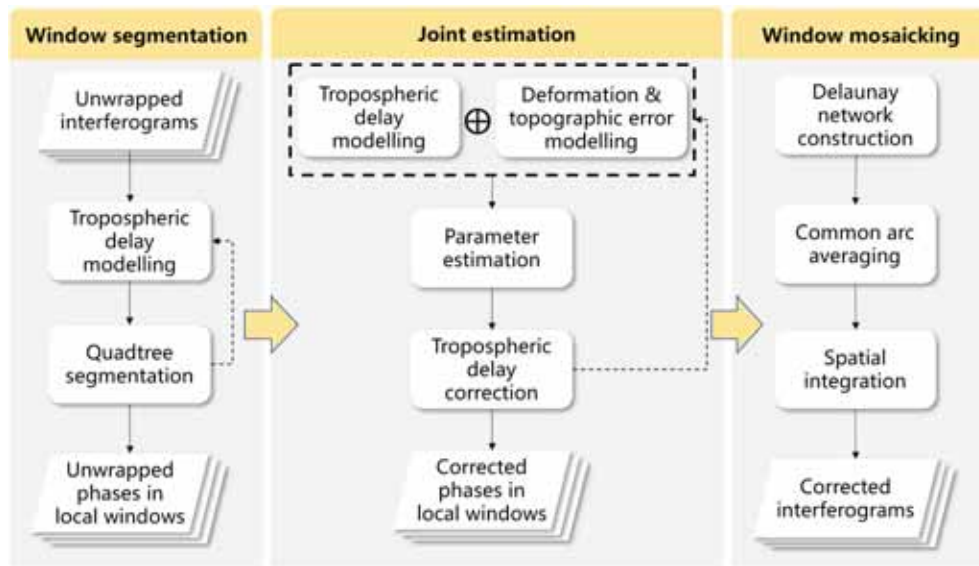


Fig. 1. The flow chart of the proposed tropospheric correction.

2.4. Local window segmentation

As described above, the elevation-dependent tropospheric delay varies significantly over large-scale areas, thus the single linear function cannot fully describe the spatial variability of troposphere over the whole interferogram. Although previous studies have attempted to mitigate the heterogenous effect by segmenting the interferogram into predefined windows (Bekaert et al., 2015; Liang et al., 2019), the definition of window size largely relies on the experience of the InSAR operators. In a smaller window there might be insufficient observations for reliable estimation which can lead to overfitting of turbulence, while within a larger window, the spatial variability of the troposphere can prevent accurate modelling. To balance the computation efficiency and the fitting accuracy, we propose an adaptive segmentation based on the statistics of phase variations. We first assume the phase variation is mainly attributed to tropospheric delay. For m interferograms, the overall phase variation is modelled as a function of tropospheric delay,

$$\Phi = \mathbf{B}_{trop} \cdot \mathbf{P}_{trop} + \mathcal{E} \quad (17)$$

where \mathcal{E} represents a vector of phase residuals that contain deformation, topographic error and unmodelled tropospheric delay. If the phase variation cannot be fully described by Eq. (2), the window needs to be further divided into smaller windows. In this context, we adopt the quadtree strategy to divide the windows. Accordingly, the size of the divided window is determined by two threshold values, i.e., the fitting degree of tropospheric delay model and the predefined minimum window size. The former is defined by the phase standard deviation (STD) of the temporally averaged interferogram. Because the atmospheric noise in the averaged interferogram is reduced by \sqrt{m} times (Zebker et al., 1997), the phase variation in the averaged interferogram is mainly contributed by the deformation signal. If the STD of \mathcal{E} is larger than the STD threshold, the window is further divided into quadrant windows until the size of the divided window reaches the threshold of minimum window size. The window size threshold can be determined by either a priori knowledge or a tradeoff between the resulting fit to the phase and the number of windows, such as using L-curve method based on phase misfit STD (Murray et al., 2020).

2.5. Practical considerations

It should be noted that the computational burden of this method can become high, particularly in a large-scale area with abundant

interferograms and dense coherent points. To reduce the computation burden, the multi-reference interferograms can be converted to consecutive interferograms before the tropospheric correction. Because the contributed signals (i.e., deformation, topographic error, tropospheric delay, etc.) within interferograms fulfill the closure condition over a closed interferogram loop (Agram and Simons, 2015), the conversion can be achieved via least squares or singular value decomposition (Berardino et al., 2002; Liang et al., 2021). It is worth noting that the conversion of consecutive interferograms may introduce non-closure phase bias possibly due to soil moisture (Ansari et al., 2021) and/or processing errors (Molan et al., 2020). The undesired phase bias can be mitigated by using phase linking with all possible interferograms (Ansari et al., 2021) or triplet-based correction model only with small baseline interferograms (Falabella and Pepe, 2022; Maghsoudi et al., 2022; Zheng et al., 2022).

In addition, because the tropospheric delay is modelled as the combination of X , Y , and H in Eq. (2), the intercorrelations between the variables may cause structural multicollinearity, which possibly results in unreliable estimation. In this situation, mean-centering and/or standardization of independent variables can help to lower their correlations (Kumar, 1975). The flowchart of the whole processing is drawn in Fig. 1, and the main steps are summarized as follows.

1. Model the phase variation as a function of tropospheric delay by Eq. (17).
2. Calculate the misfit STD and determine whether the window needs to be further divided into quadrant windows.
3. Repeat step 1 and 2 until the size of divided window reaches the threshold of minimum window size.
4. In each local window, model the phase variation as a combination of tropospheric delay, deformation and topographic error by Eq. (13).
5. Correct the tropospheric delay in local windows.
6. Construct Delaunay network in all local windows, smooth the inconsistency of phase differences in overlapping areas by average values.
7. Conduct spatial integration from arc to point over the whole interferograms.

It is noting that the tropospheric delay is modelled twice in the whole process. The first is to determine whether window segmentation is needed or not, while the second is to estimate tropospheric delay together with deformation and topographic error.

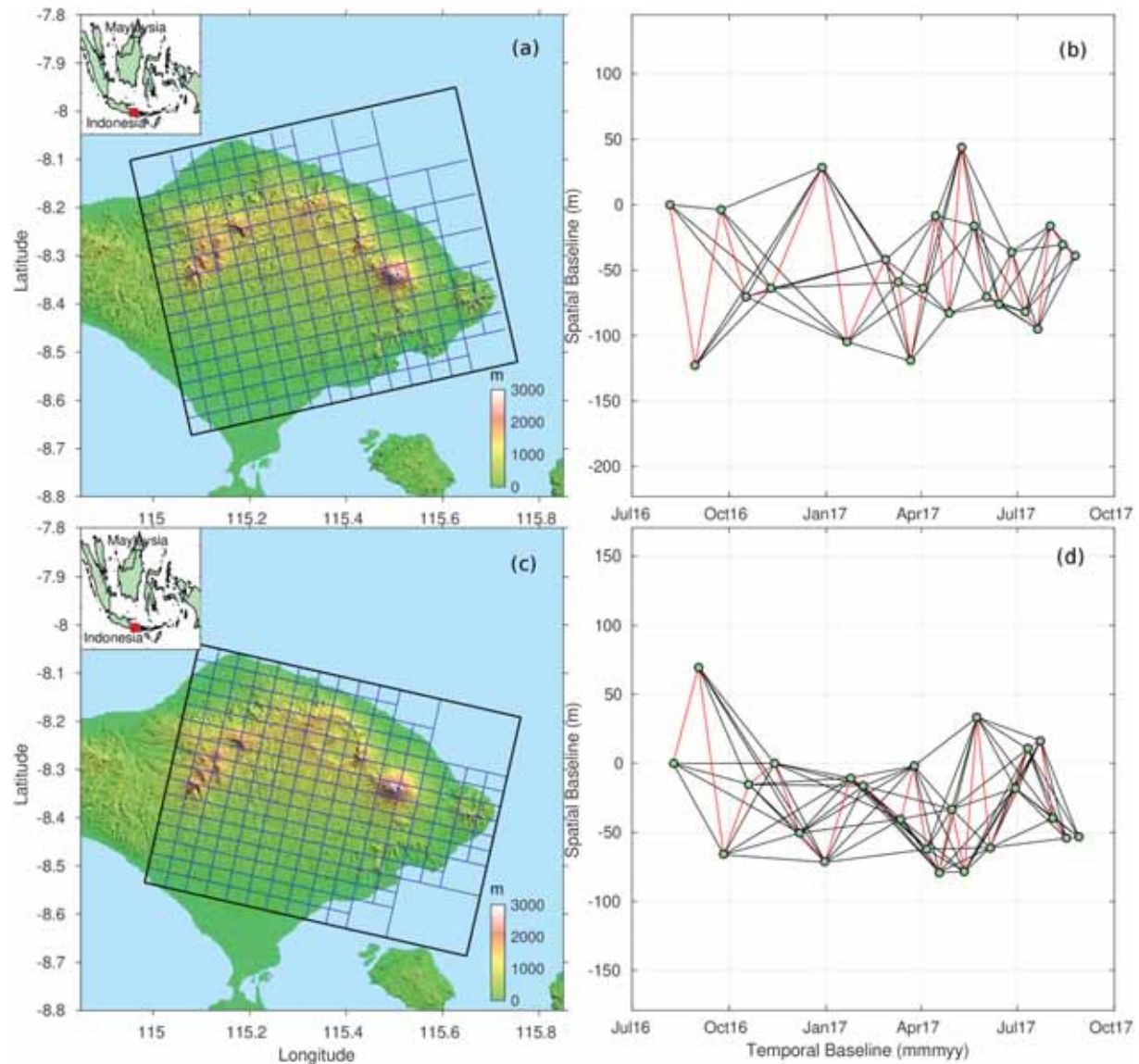


Fig. 2. (a) & (c) Overview of the study area covering the island of Bali with quadtree segmentation; (b) & (d) spatiotemporal baselines for processed Sentinel-1 datasets. Red lines represent the consecutive interferograms; (a) & (b) ascending track; (c) & (d) descending track;

3. Performance analysis of tropospheric delay correction in MTInSAR

3.1. A case study: Island of Bali

3.1.1. Reduction in phase variability

We first evaluate the performance of the proposed method at the island of Bali that hosts two active stratovolcanoes, Agung and Batur. The andesitic stratovolcano Agung show signs of reawakening in recent years. The signs of unrest include a seismic swarm and fumarole activity, which last for three months before an eruption on 21 November 2017. Batur volcano has been active in the past ~200 years with the most recent eruption in 1999–2000 (Hidayati and Sulaeman, 2013). We collect both ascending and descending Sentinel-1 SAR images over this island in the period from August 2016 to August 2017, during which the deformation of the volcano is subtle but is masked by the tropospheric delay. Based on the collected SAR images, we generate 82 ascending interferograms and 100 descending interferograms with multilook number of 20 and 4 in range direction and azimuth direction, respectively. To improve the phase quality and to determine the integer

ambiguity, we use the arc-based phase linking method proposed in Liang et al. (2021) to derive 22 unwrapped consecutive interferograms in both tracks. The tropical environment poses challenges for deformation detection due to the complex lateral variations of water vapor. In this context, we apply the proposed method to correct the tropospheric delays within interferograms and compare the outcome with two commonly used correction methods, i.e., (1) empirical linear correction based on phase-elevation correlation, and (2) weather model correction using Generic Atmospheric Correction Online Service (GACOS) (Yu et al., 2018). During the quadtree segmentation, the thresholds of residual STD are determined as 0.14 rad (ascending track) and 0.11 rad (descending track) by computing the temporal stacking interferograms. The lower bounds of the segmentation window size are determined as 4 km for both tracks. The segmented window distributions are overlaid on Fig. 2a and Fig. 2c.

Fig. 3 and Fig. 4 show examples of tropospheric correction by the three methods in ascending track and descending track, respectively. As expected, the interferometric phases in tropical regions are dominated by elevation-dependent tropospheric delays and lateral variations, highlighting the importance of tropospheric correction. After correction

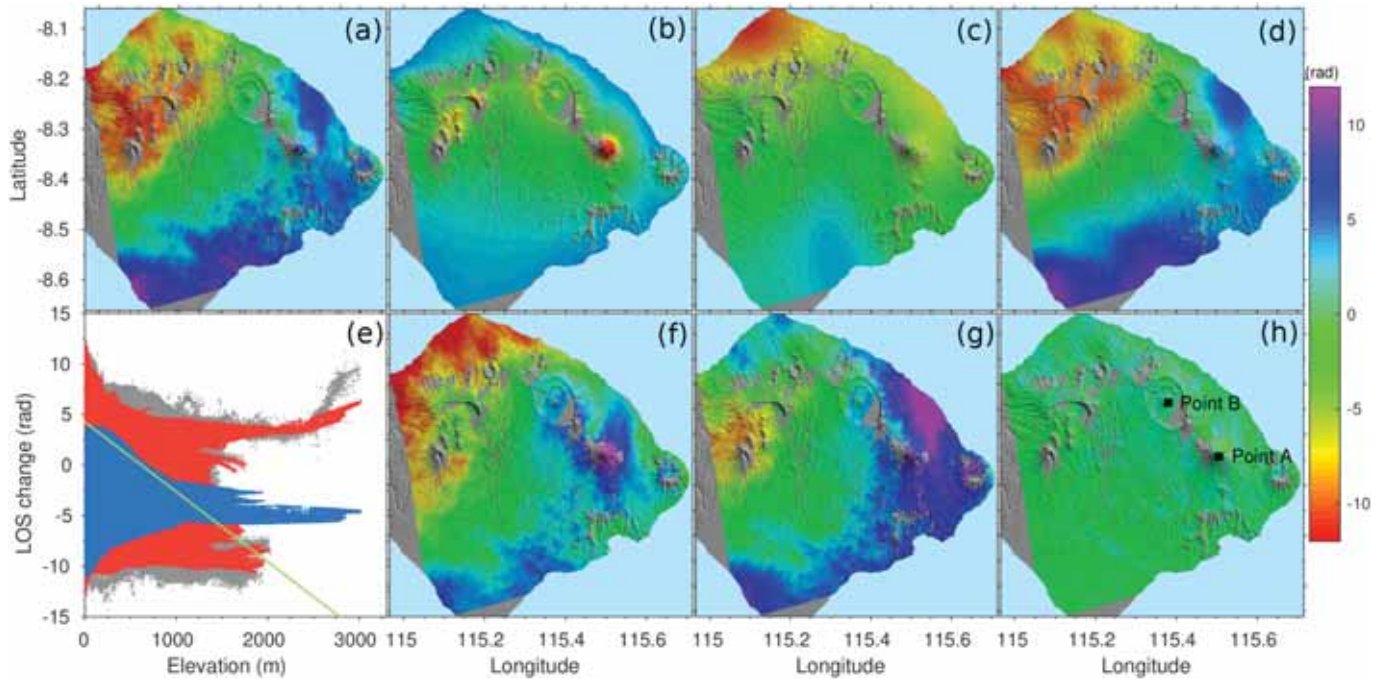


Fig. 3. (a) Example of uncorrected interferogram in ascending track (20170509–20170521); delay phases estimated by (b) linear method; (c) GACOS model; (d) the proposed method; (e) elevation versus phases for the uncorrected interferogram (gray), the linear estimation (green), GACOS estimation (blue), and the joint model estimation (red); (f-h) residual phase maps after the respective corrections shown in (b-d). (For interpretation of the references to colour in this figure legend, the reader is referred to the web version of this article.)

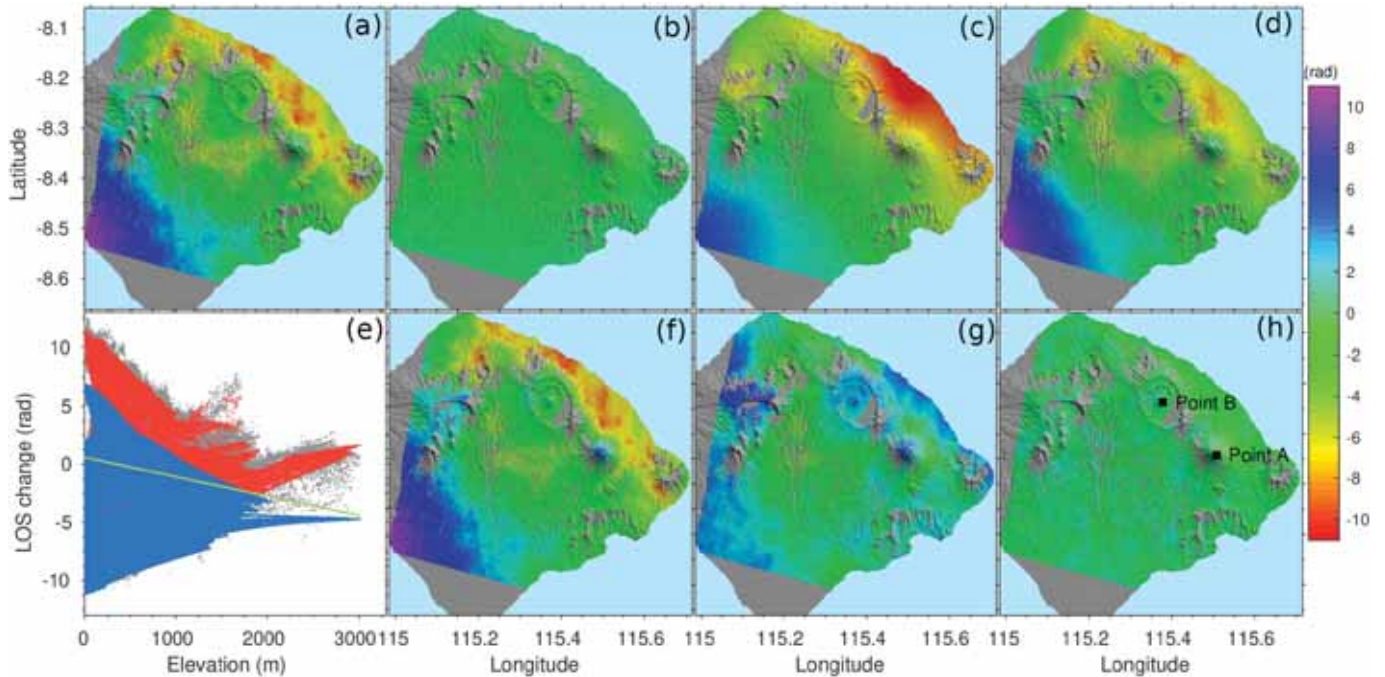


Fig. 4. (a) Example of uncorrected interferogram in descending track (20160902–20160926); delay phases estimated by (b) linear method; (c) GACOS method; (d) the proposed method; (e) elevation versus phases from the uncorrected interferogram (gray), the linear estimation (green), GACOS estimation (blue), and the proposed estimation (red); (f-h) residual phase maps after the respective corrections. Point A and B are located at the centers of volcanic peaks, Agung and Batur, respectively. (For interpretation of the references to colour in this figure legend, the reader is referred to the web version of this article.)

by the three methods, they all cause reduction in spatial variability of phases to some degree. For the linear correction, the standard deviation (STD) of interferogram phase decreases from 5.71 rad to 5.12 rad in ascending track and from 4.31 rad to 4.23 rad in descending track. For GACOS, the phase STD decreases from 5.71 rad to 4.75 rad in ascending

track and from 4.31 rad to 2.07 rad in descending track. Although GACOS method performs better than the linear approach, they both remove a small portion of tropospheric delays in interferograms. It is not surprising that the proposed method, which accounts for the spatial variability by quadtree segmentation, largely reduces the local phase

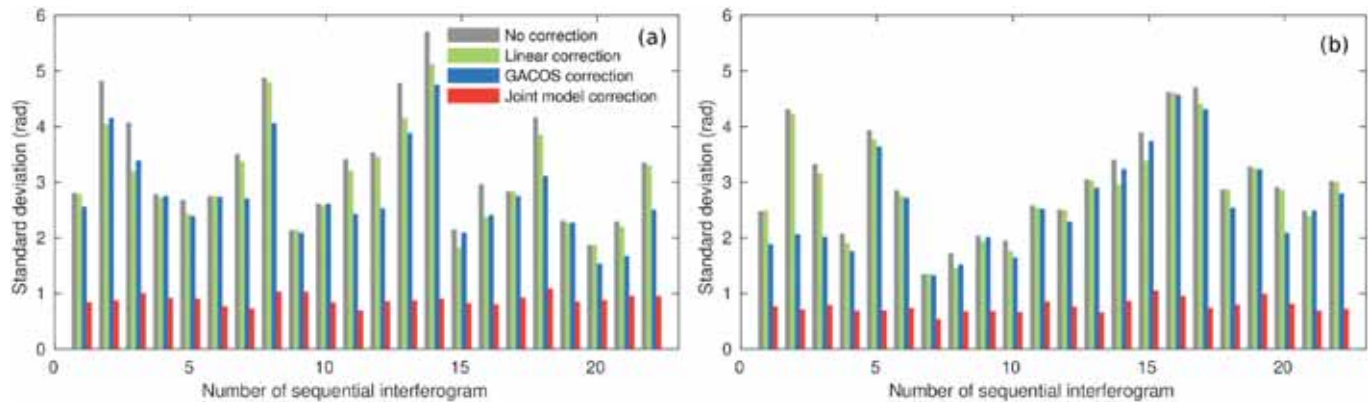


Fig. 5. Standard deviation statistics of consecutive interferograms before and after tropospheric corrections for ascending track (a) and descending track (b), respectively.

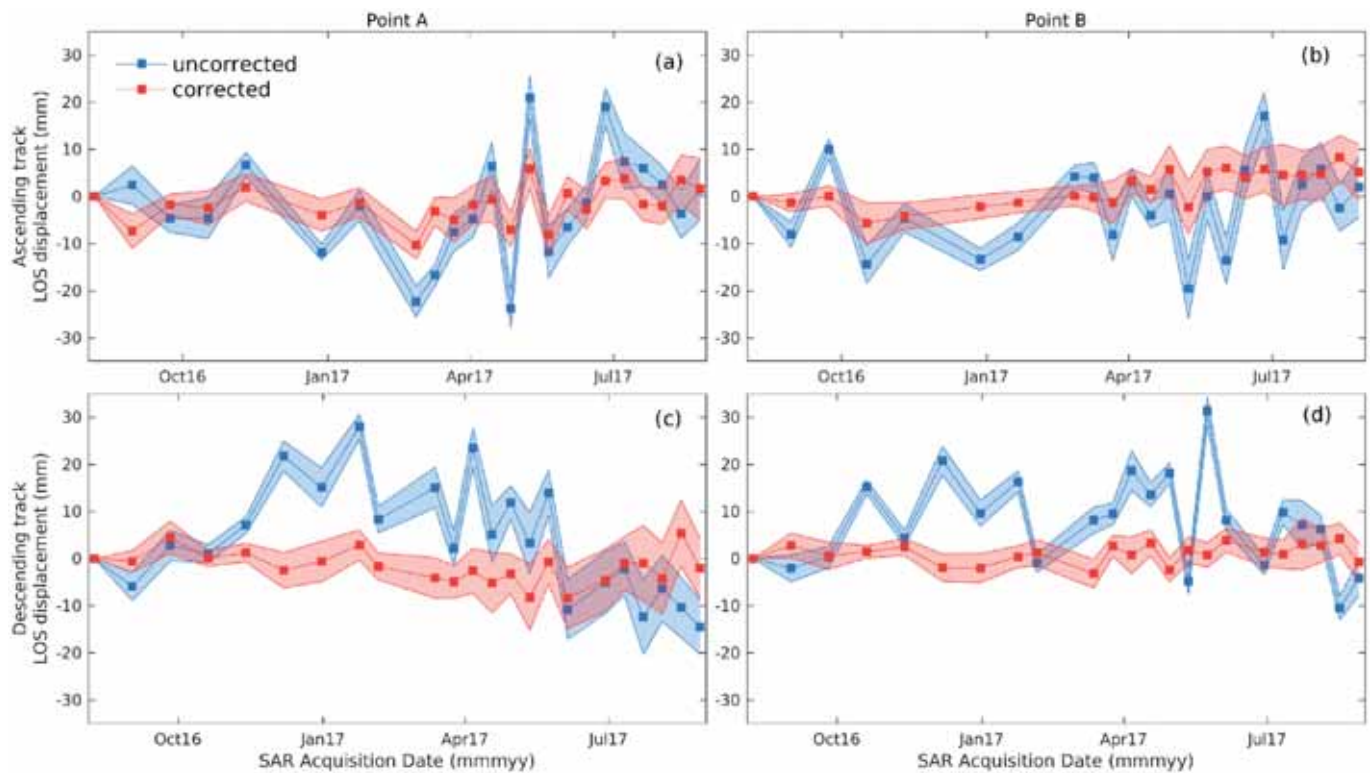


Fig. 6. LOS time-series displacement comparison of point A (a & c) and B (b & d) before and after tropospheric correction. (a & b) ascending track; (c & d) descending track. The shaded area represents the standard deviation calculated within a 500 m window surrounding the central point at each epoch.

variations with lower standard deviations of 0.91 rad in ascending track and 0.71 rad in descending track. Looking further at the STD statistics for all involved interferograms (Fig. 5), in the results from linear method and GACOS method, some interferograms after tropospheric correction still show large phase variability. This is because the spatiotemporal variability of tropospheric properties might be too complex so that they cannot be fully described by global linear model or weather model. In contrast, the proposed correction method achieves large reductions in phase STD with less than 1 rad for all interferograms. The remaining phase residuals are likely caused by localized turbulence, unmodelled deformation, and decorrelation noise.

3.1.2. Reduction in displacement fluctuation

To assess the impact of the tropospheric delay on deformation retrieval, we compare the time-series displacements from August 2016

to August 2017 with and without tropospheric delay correction. As the Agung volcano and the Batur volcano at Bali island experience decades of quiescence before the active seismic swarm, and the deformation in the observation period is considered to be stable (Albino et al., 2019). Fig. 6 shows the time-series line-of-sight (LOS) displacements at two selected points that are located at the centers of Agung volcano and Batur volcano. We can see that the uncorrected time-series displacements show large fluctuations caused by the tropospheric delay, hampering the extraction of ground deformation trend. After correction by the proposed method, the amplitude of temporal variation in displacement is largely reduced, thus enabling a more accurate interpretation for the volcanic activities.

3.1.3. Semi-experiment in separation between the coupled signals

As mentioned, the empirical linear phase-elevation correction can

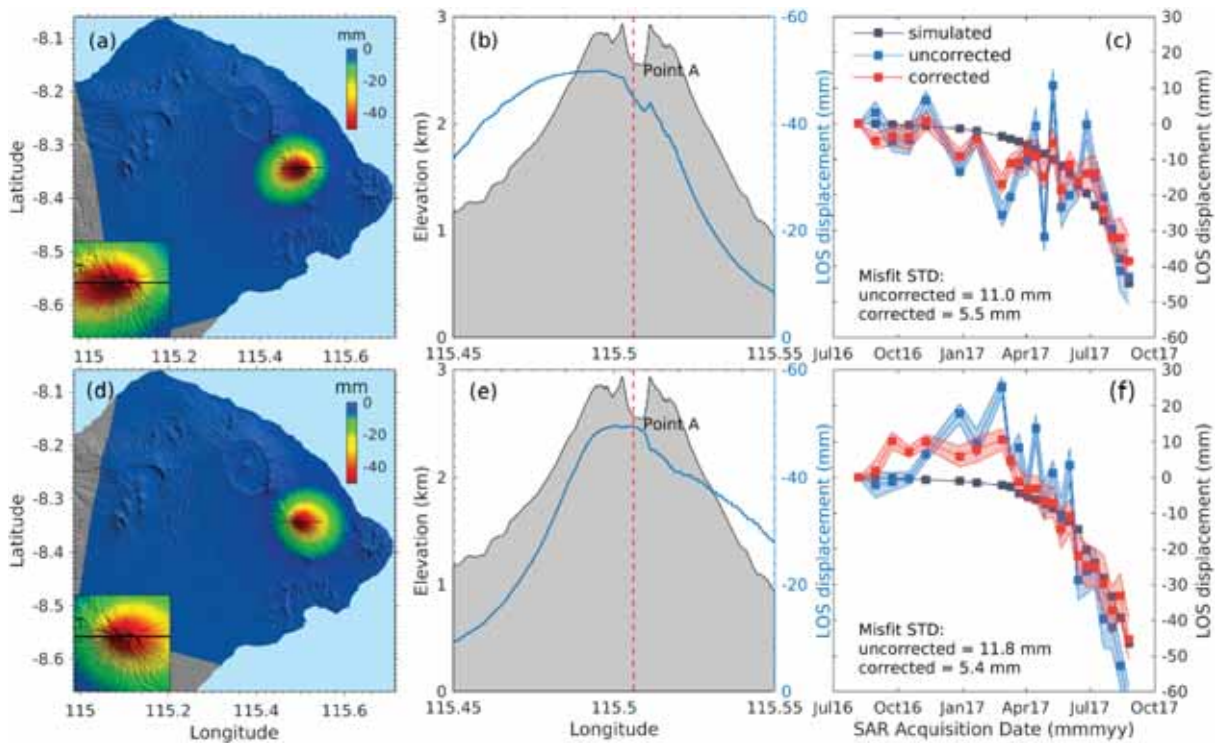


Fig. 7. (a & d) Simulated displacement maps using Mogi model; (b & e) schematic diagram of correlation between elevation and simulated deformation signal; (c & f) comparison of LOS time-series displacements before and after tropospheric correction at point A. The black lines represent the simulated displacements, the blue lines represent the uncorrected displacements, and the red lines represent the displacements after joint model correction. (a, b, c) ascending track; (d, e, f) descending track.

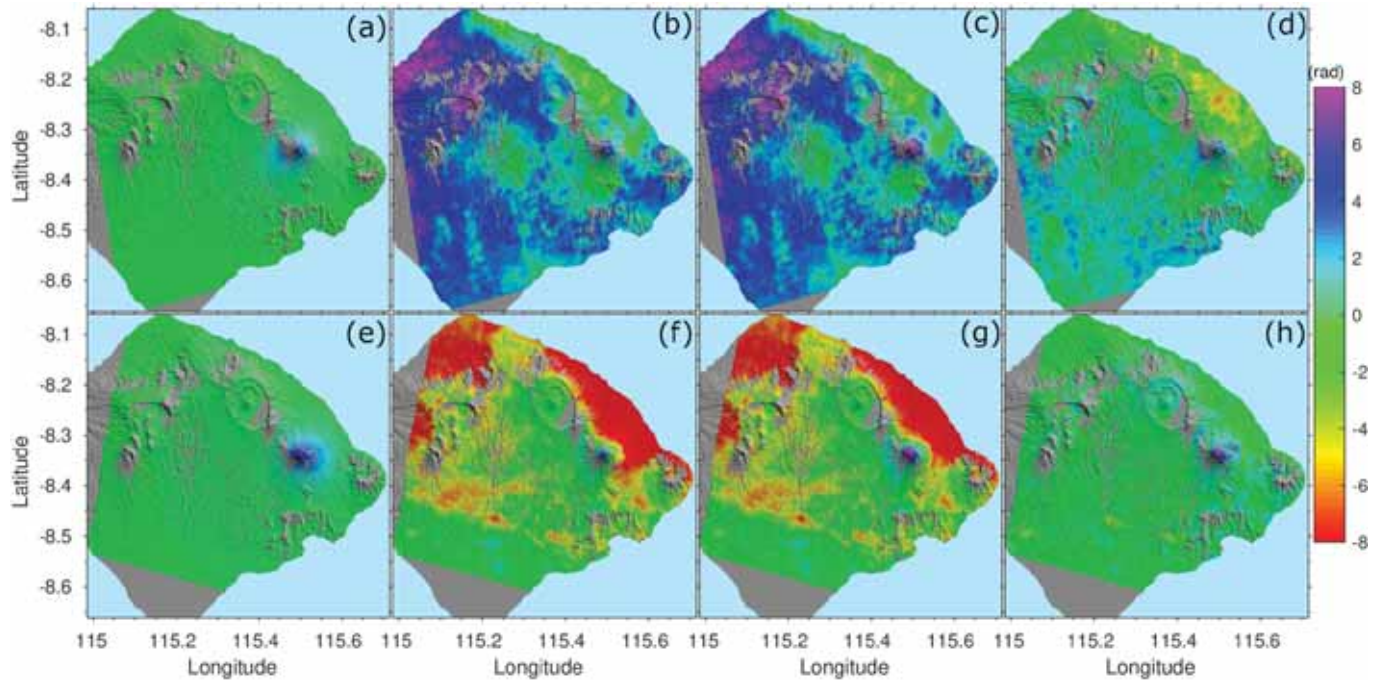


Fig. 8. (a & e) Simulated interferograms containing only deformation signals; (b & f) original interferograms; (c & f) interferograms by combining original phases and simulated deformation signals; (d & h) interferograms after tropospheric correction by the proposed method; (a, b, c & d) ascending track interferogram (20170708–20170813); (e, f, g & h) descending track interferogram (20170711–20170828). To illustrate the deformation signal more clearly, interferograms with long temporal baselines are selected.

partially remove the true deformation signal if the deformation pattern is correlated with elevation. The erroneous removal is quite common in situation of volcanic inflation and deflation. To validate whether the

proposed method can avoid the mistake, we simulate a scenario where the elevation-correlated deformation is included in the interferograms. We use Mogi model (Mogi, 1958) to generate a deformation field that

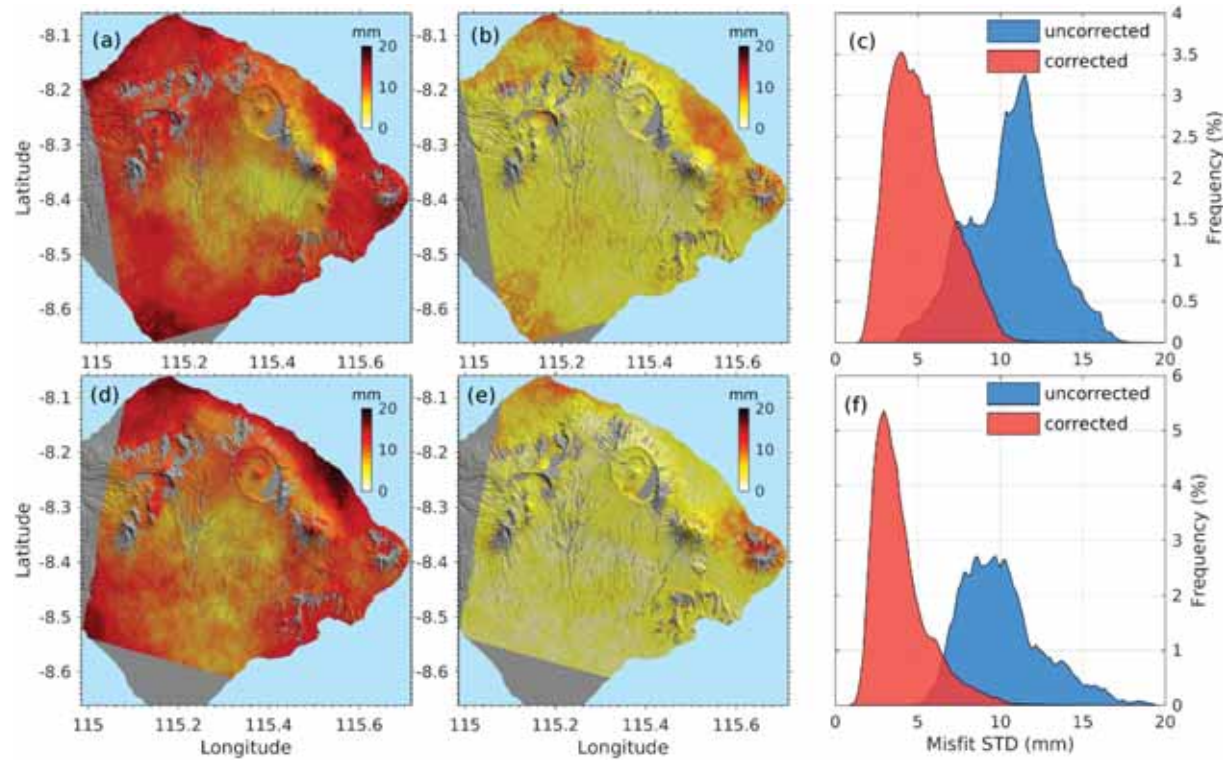


Fig. 9. Maps of deformation misfit STD before (a & d) and after (b & e) tropospheric corrections using simulated deformation map as reference. (c & f) histograms of the phase STD. (a, b, c) ascending track; (d, e, f) descending track.

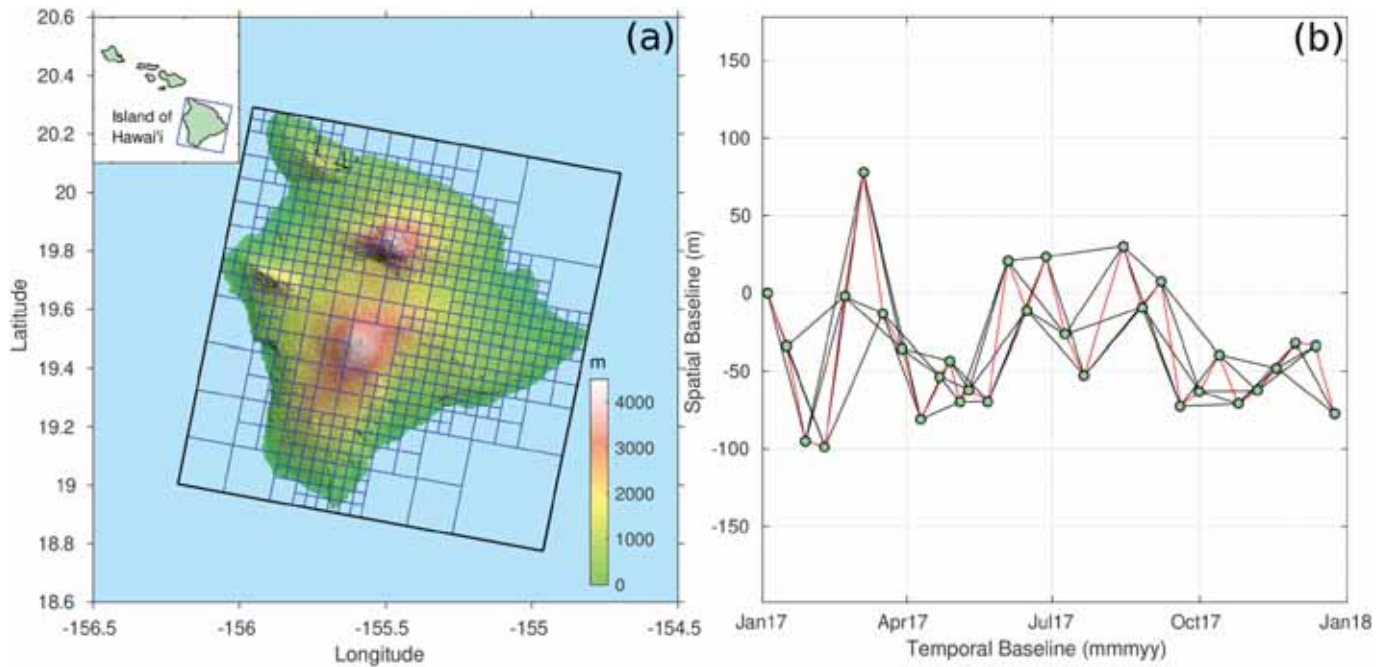


Fig. 10. (a) Overview of the study area covering the island of Hawaii with quadtree segmentation; (b) spatiotemporal baselines for processed Sentinel-1 dataset. Red lines represent the consecutive interferograms. (For interpretation of the references to colour in this figure legend, the reader is referred to the web version of this article.)

has nonlinear temporal variation at the volcanic edifice of Agung (Fig. 7). Fig. 8 displays examples of simulated interferograms and tropospheric corrections in ascending track and descending track, respectively. It can be seen that, despite that the elevation-correlated deformation and tropospheric delay are coupled in space, they still

can be separated based on their temporal properties. The simulated time-series displacements are well preserved with a 50% reduction of misfit STD after adopting the proposed correction (Fig. 7 c & f). We further calculate the misfit STDs for all pixels in space. As shown in Fig. 9), the average misfit STD decreases from 10.6 mm to 5.2 mm for

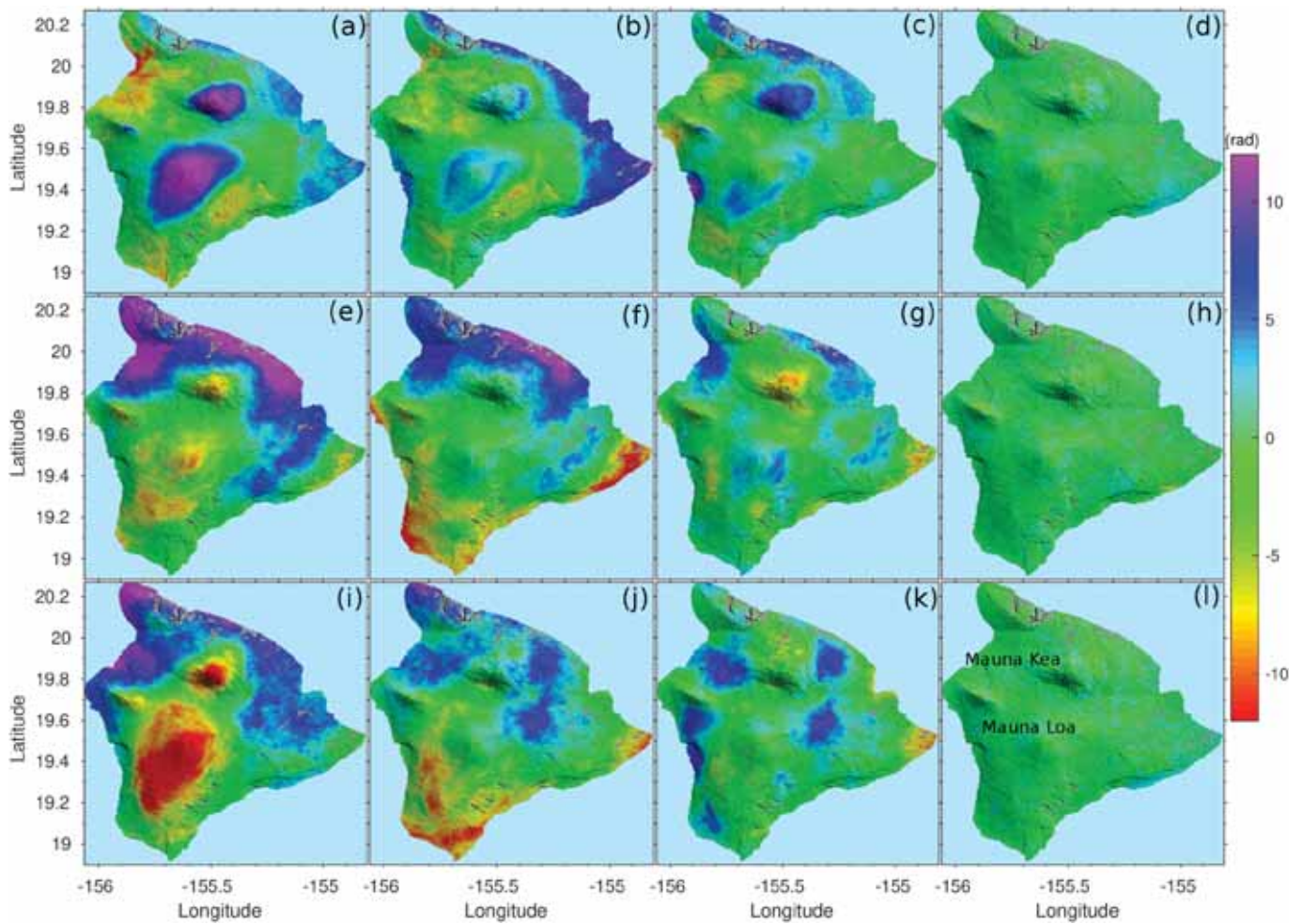


Fig. 11. Examples of uncorrected interferograms (a, e, i), and residual phase maps after linear correction (b, f, j), GACOS correction (c, g, k), and the proposed correction (d, h, l) for 20,170,615–20,170,627 (top row), 20,171,001–20,171,013 (middle row), and 20,171,118–20,171,130 (bottom row).

ascending track and from 10.1 mm to 4.0 mm for descending track, respectively. The percentages of STD decrease in both tracks exceed 50%. The results suggest that the proposed method can separate the tropospheric delay from the deformation even though the two signals have a strong correlation in space. Note that the remaining misfit STDs, especially the relatively large values (10 mm) at the east coastline and

mountainous area are possibly due to localized turbulence which cannot be fully described by quadtree segmentation and trilinear function.

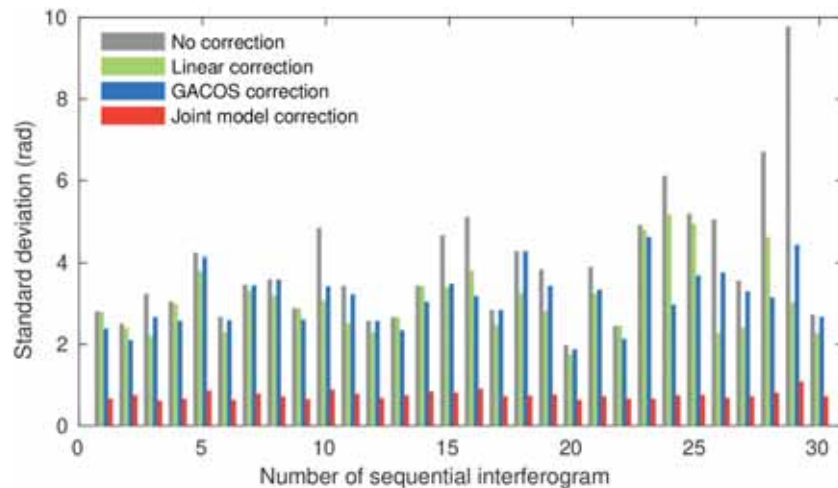


Fig. 12. Standard deviation statistics of consecutive interferograms before and after tropospheric corrections.

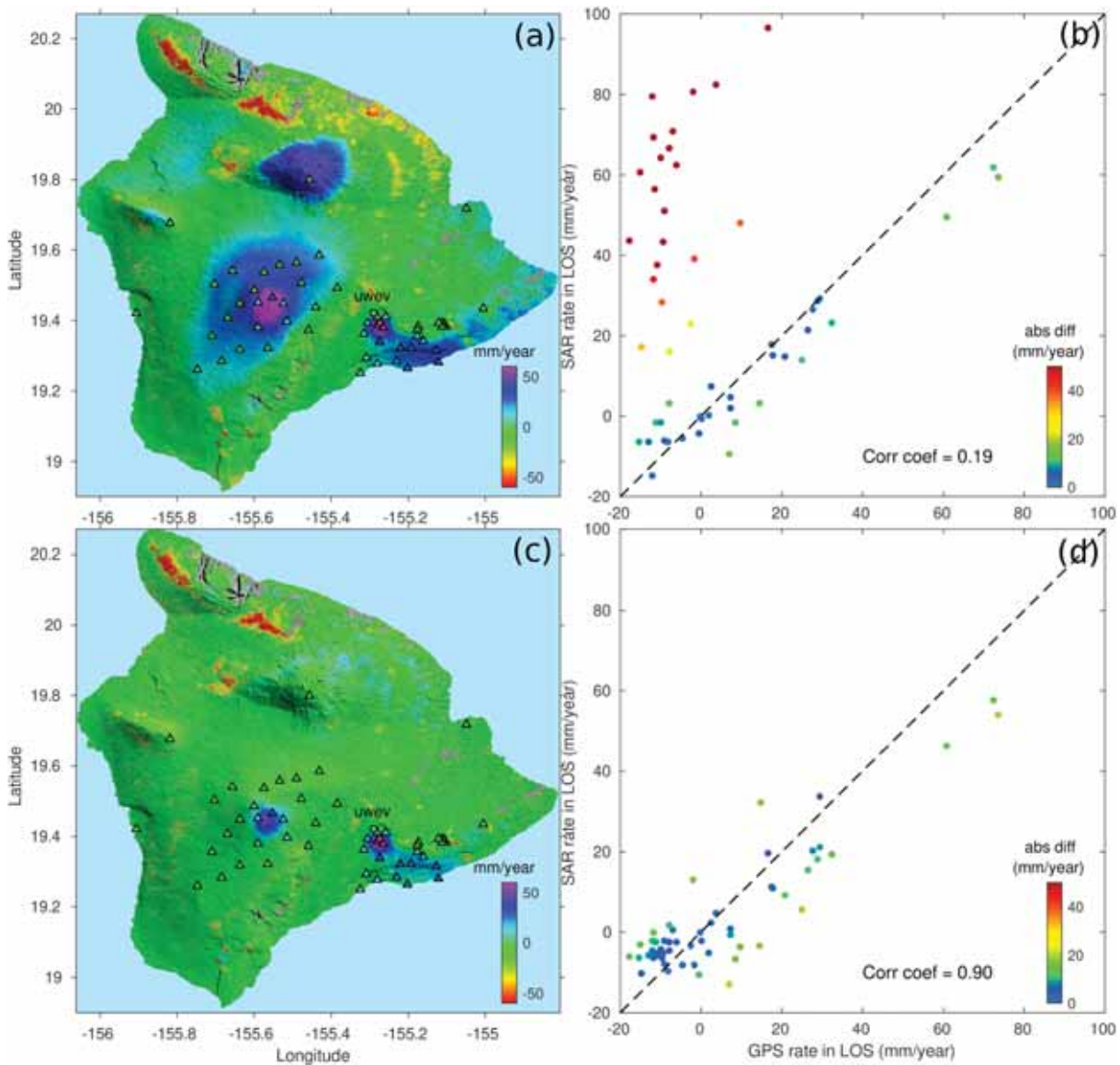


Fig. 13. GPS locations (triangles) overlapped on the InSAR deformation rate maps before (a) and after (c) tropospheric correction at the island of Hawaii. GPS site (uwev) corresponds to the reference site (rectangular). InSAR rates versus GPS rates before (b) and after (d) tropospheric correction.

3.2. A case study: Island of Hawaii

3.2.1. Reduction in phase variability

The second case study is conducted at the island of Hawaii (Fig. 10a), home to Kilauea volcano, one of the most active volcanoes in the world. We collect 32 Sentinel-1 descending SAR images spanning from January to December 2017. After co-registration process, the SAR images are used to generate 87 interferograms with multilook number of 20 and 4 in range direction and azimuth direction, respectively, resulting in a spatial resolution of around 80 m. The multi-reference interferograms are unwrapped and converted to 31 consecutive interferograms (Fig. 10b). Then the proposed method is adopted to correct the tropospheric delays in the interferograms. During the quadtree segmentation, the STD threshold and minimum size of divided window are determined as 0.14 rad and 4 km, respectively (Fig. 9a). The resulting interferograms are shown in Fig. 11, where the interferograms are corrected by the linear method, GACOS and the proposed method. It can be observed that the linear method and GACOS cannot fully remove the tropospheric delay patterns in space, leading to undesirable deformation results. The proposed method produces significant reductions in both elevation-

correlated and lateral phase variations. Looking into the phase STD statistics of all interferograms (Fig. 12), it is noted that the conventional methods can only account for the phase variations in a portion of interferograms, while the proposed method works for all interferograms because their phase STDs are all reduced.

3.2.2. Reduction in displacement fluctuation

The GPS measurements provided by the Nevada Geodetic Laboratory (NGL) (Blewitt et al., 2018) are used to validate the deformation retrieval from InSAR. Before projecting the GPS displacements onto LOS direction, we remove the tectonic movement trend in the GPS measurements. Then InSAR and GPS displacements are referenced to the first SAR acquisition in time and a GPS station (uwev) in space. The comparison between InSAR and GPS deformation rate is presented in Fig. 13. We find that, before the tropospheric correction, the elevation-correlated ramp causes false uplift at Mauna Kea and Mauna Loa. The false uplift results in a low correlation value (0.19) between InSAR and GPS rate measurements. After tropospheric correction by the proposed method, the false uplift signal is removed, leading to a noticeable increase of correlation value (0.9). This result suggests the importance of

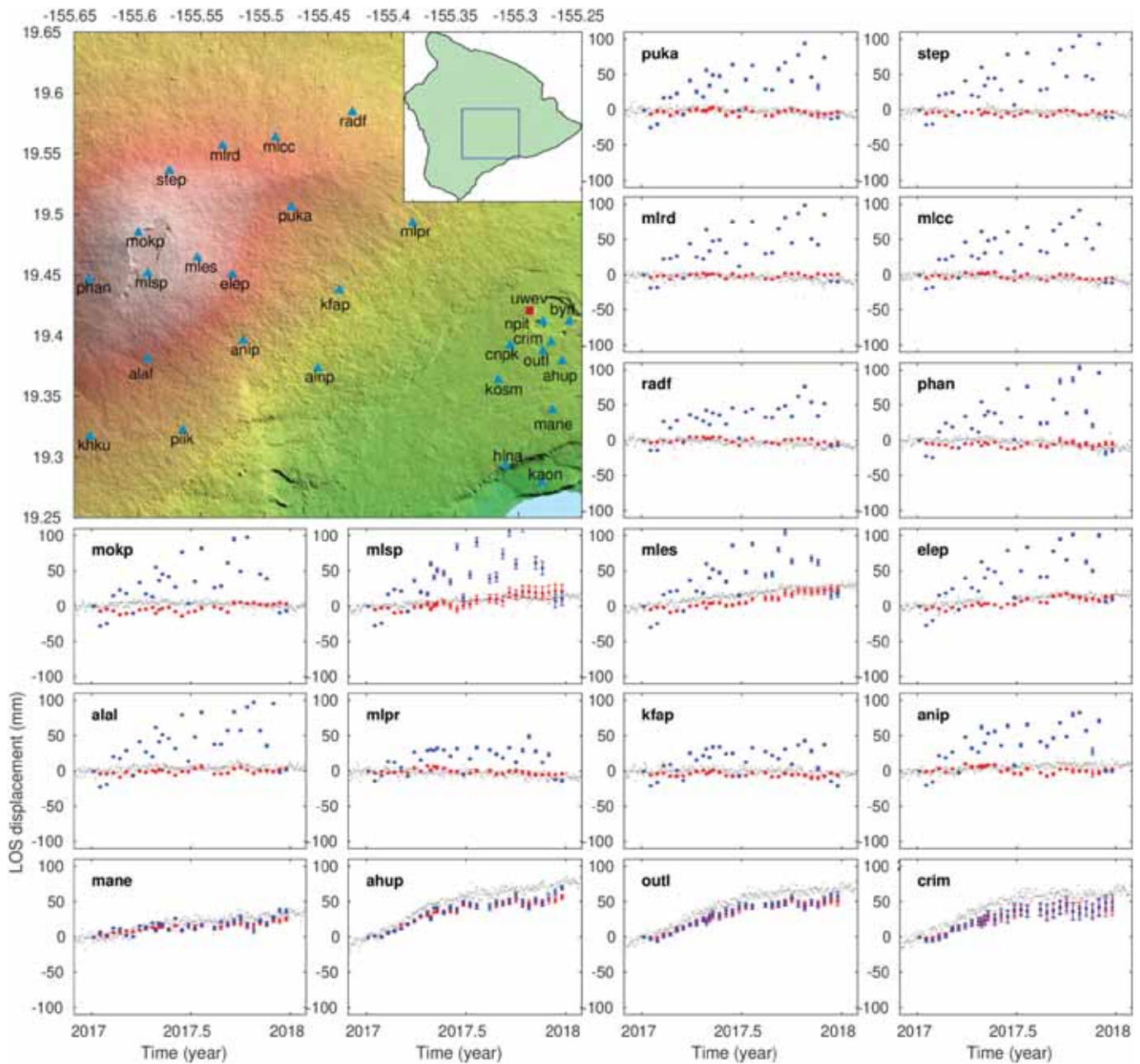


Fig. 14. Comparison of LOS time-series displacements at GPS sites (locations (triangles) shown in upper left, red rectangular (uwev) corresponds to the reference site). GPS measurements (gray) are plotted with the uncorrected (blue) and corrected (red) InSAR displacements. (For interpretation of the references to colour in this figure legend, the reader is referred to the web version of this article.)

tropospheric correction in volcanic areas. We further compare the time-series displacements for InSAR and GPS at selected GPS sites (Fig. 14). It can be seen that the temporal variability of InSAR displacements is reduced after applying the proposed tropospheric correction. The average misfit STD decreases from 25.1 mm to 4.5 mm. The improvement of InSAR deformation retrieval could facilitate interpretation and early warning of magma transport and volcanic eruption in future.

We notice that the subsidence phenomena at the northwestern corner of the island is preserved after the tropospheric correction. To examine whether the deformation pattern is caused by turbulence, we analyze the time-series displacements in these areas. The results are presented in Fig. 15, it is observed that before the tropospheric correction, there is a downward trend in the time-series displacements at the mountainous terrains of the northwestern corner. However, their temporal evolutions are contaminated by the tropospheric delays, leading to

severe fluctuations, which are demonstrated by the nearby GPS displacements at Mauna Kea (Fig. 15c). Through the proposed tropospheric correction, the undesired temporal variation is largely alleviated, showing a consistent movement. This result suggests that the proposed method has ability to mitigate the tropospheric delay and meanwhile preserve the underlying ground movement signals.

3.2.3. Comparison with GPS zenith delay

Considering that the NGL provides zenith delay products every 5 min from the GPS stations, we compare the GPS-derived Zenith Total Delay (ZTD) against the GACOS-derived and the InSAR-derived ZTDs. The comparison at GPS stations is presented in Fig. 16. It can be seen that the ZTDs derived from the proposed method fit well with those derived from GPS measurements, verifying the effectiveness of the proposed method. Taking the GPS-derived ZTDs as reference values, we then calculate the

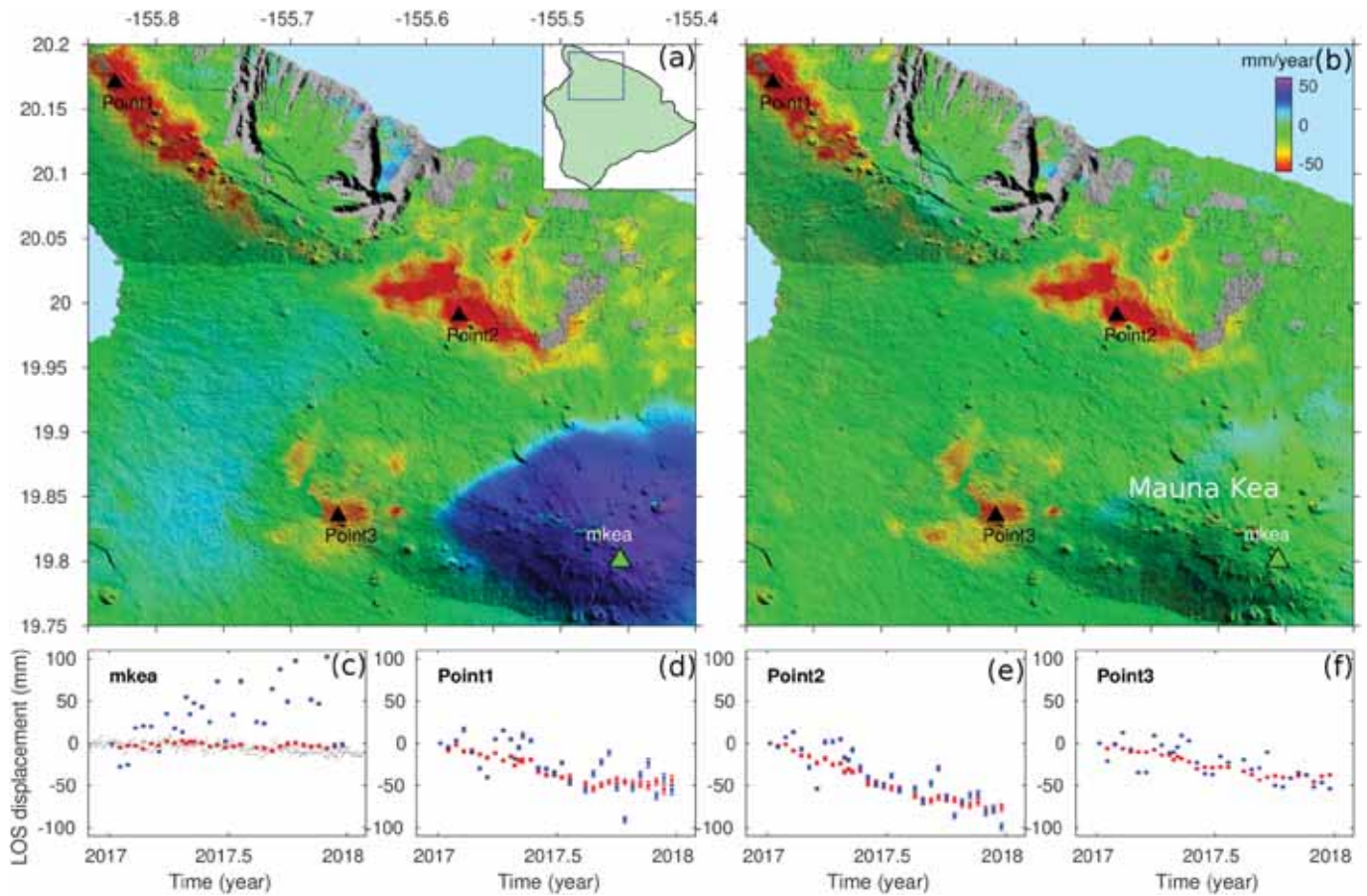


Fig. 15. Comparison of InSAR deformation rate (a) before and (b) after tropospheric correction at the mountainous terrains of the northwestern corner. (c-f) Comparison of LOS time-series displacements at selected sites.

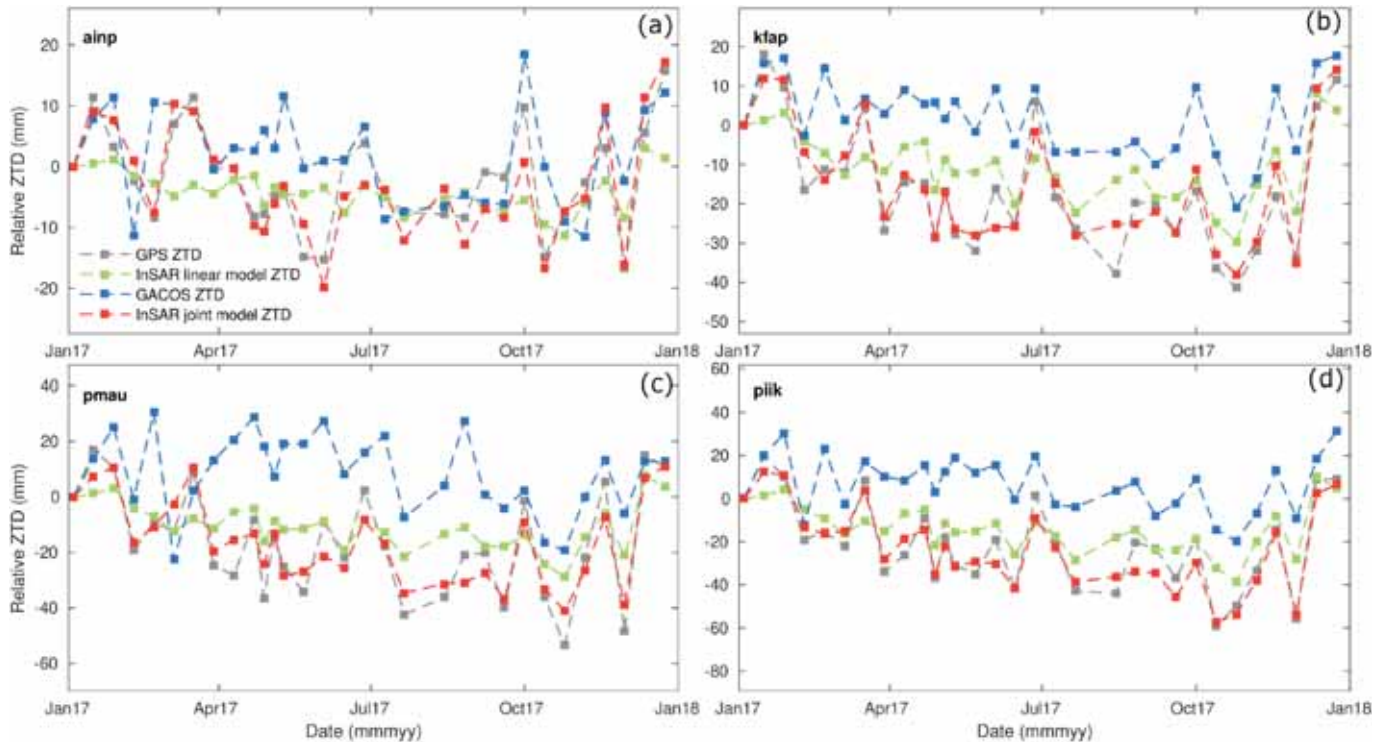


Fig. 16. Comparison of temporal ZTDs between GPS and those from InSAR and the GACOS measurements, respectively. All ZTD values are referenced to the first SAR acquisition in time and an arbitrarily selected GPS station (uuev) in space.

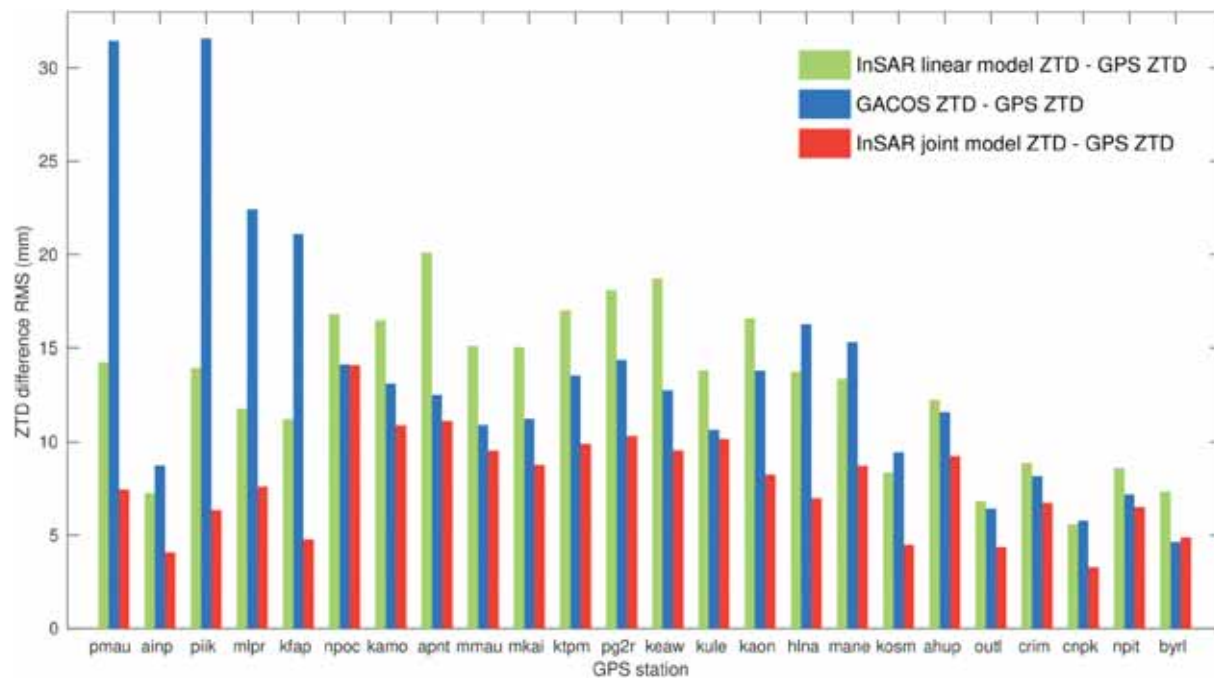


Fig. 17. RMS statistics of ZTDs from our methods and the GACOS at GPS stations using the GPS ZTDs as reference values.

Table 1
Cumulative running time of the proposed method in three data sets.

Data set	Data size (number of interferogram/ point)	Running time (min)
Bali island (ascending)	22/689350	6.2275
Bali island (descending)	22/705026	6.3437
Hawaii island (descending)	30/2391225	43.0863

root-mean-square (RMS) of the GACOS-derived and the InSAR-derived ZTDs, respectively. Fig. 17 presents the RMS statistics at all 24 GPS stations. This result indicates that the proposed method possesses a lower RMS with an average value of 7.8 mm compared with GACOS. The biases are mainly attributed to the turbulent artifacts and the spatio-temporal inconsistency between InSAR and GPS observations.

3.3. Computation efficiency

In order to assess the computation efficiency, the cumulative processing time for each of the three datasets is provided in Table 1. The operating environment is MATLAB in a workstation with Intel Xeon CPU and 384 GB memory. To ensure a fair assessment, the pre-processing steps (e.g., phase unwrapping and interferogram conversion) have been excluded when counting the running time. From Table 1, it can be seen that the processing time of the new method is relatively long, especially for the entire scene with hundreds of interferograms. The high demand for time is mainly attributed to the joint estimation of intensive parameters. However, considering the by-products, e.g., deformation and topographic error, are simultaneously obtained, the computation cost is acceptable.

4. Conclusion and discussion

Tropospheric delay is one of the main impediments to deformation retrieval from InSAR measurements. Accurate separation of tropospheric delay from deformation field has long been a challenging issue. In this study, we provide a generic solution aiming to tackle the two

intractable issues in conventional tropospheric correction methods, i.e., the spatial variability of tropospheric properties and the coupling between deformation and topography. We first develop a quadtree segmentation strategy to mitigate the spatial variability of troposphere based on the statistics of phase variations instead of empirical settings. The coupling effect between deformation and elevation-dependent tropospheric delay is reduced by exploring their distinct temporal characteristic and jointly modelling.

We validate the effectiveness of the proposed method over the islands of Bali and Hawaii, where the volcanic displacements are obscured by tropospheric delays. At Bali island, the misfit STDs from simulated displacements are reduced by ~50% after applying the proposed correction. At Hawaii island, the average misfit STD between InSAR and GPS displacements decreases from 25.1 mm to 4.5 mm through the proposed correction. The experimental results also demonstrate that the method can separate tropospheric delay from deformation even though the two signals have a strong correlation.

It should be noted that the temporal correlation assumption for deformation holds in most cases, but there are exceptions that the transient deformation signal is temporally uncorrelated, such as co-seismic deformation. The model unfitting would degrade the accuracy of tropospheric delay estimation. This is the potential limitation of the method. Nevertheless, one possible solution to this problem is to divide the interferogram stack into two sub-stacks by setting the transient deformation event as a midpoint. Then the proposed method is adopted separately in each sub-group of interferograms where deformation signal is considered to be temporally correlated.

Another limitation of this proposed method is the computation burden for large volume data. As the tropospheric correction in local windows is independent, our future work is to build a parallel processing framework which is expected to enhance the algorithm efficiency especially for big SAR data processing.

CRediT authorship contribution statement

Hongyu Liang: Conceptualization, Methodology, Software, Writing – original draft. **Lei Zhang:** Conceptualization, Methodology, Writing – review & editing. **Zhong Lu:** Supervision, Methodology, Writing –

review & editing. **Xin Li:** Software, Writing – review & editing.

Declaration of Competing Interest

The authors declare that they have no known competing financial interests or personal relationships that could have appeared to influence the work reported in this paper.

Data availability

Data will be made available on request.

Acknowledgements

This work is supported in part by the National Key Research and Development Project of China (Grant No. 2021YFC3000402), in part by the National Natural Science Foundation of China (Grant No. 42174005 and 42204023), in part by the Shanghai Pujiang Program (Grant No. 21PJ1412900) and in part by the Fundamental Research Funds for the Central Universities (Grant No. 22120210520). Sentinel-1 SAR images used in this study were provided by the European Space Agency (ESA), and downloaded through the Alaska Satellite Facility (ASF) at <https://vertex.daac.asf.alaska.edu>. Atmospheric delay maps were downloaded via the Generic Atmospheric Correction Online Service for InSAR (GACOS) (<http://www.gacos.net/>). The GPS data were downloaded from Nevada Geodetic Laboratory at <http://geodesy.unr.edu>. The manuscript was greatly improved following comments by four referees and Prof. Yong Wang, the associate editor of RSE.

References

- Agram, P.S., Jolivet, R., Riel, B., Lin, Y.N., Simons, M., Hetland, E., Doin, M.P., Lasserre, C., 2013. New radar interferometric time series analysis toolbox released. *Eos, Trans. Am. Geophys. Union* 94 (7), 69–70.
- Agram, P.S., Simons, M., 2015. A noise model for InSAR time series. *J. Geophys. Res. Solid Earth* 120 (4), 2752–2771.
- Albino, F., Biggs, J., Syahbana, D.K., 2019. Dyke intrusion between neighbouring arc volcanoes responsible for 2017 pre-eruptive seismic swarm at Agung. *Nat. Commun.* 10 (1), 748.
- Ansari, H., Zan, F.D., Parizzi, A., 2021. Study of systematic bias in measuring surface deformation with SAR interferometry. *IEEE Trans. Geosci. Remote Sens.* 59 (2), 1285–1301.
- Bekaert, D., Hooper, A., Wright, T., 2015. A spatially variable power law tropospheric correction technique for InSAR data. *J. Geophys. Res. Solid Earth* 120 (2), 1345–1356.
- Berardino, P., Fornaro, G., Lanari, R., Sansosti, E., 2002. A new algorithm for surface deformation monitoring based on small baseline differential SAR interferograms. *IEEE Trans. Geosci. Remote Sens.* 40 (11), 2375–2383.
- Berrada Baby, H., Gole, P., Lavergnat, J.J.R.S., 1988. A model for the tropospheric excess path length of radio waves from surface meteorological measurements. *23 (6)*, 1023–1038.
- Bevis, M., Businger, S., Herring, T.A., Rocken, C., Anthes, R.A., Ware, R.H., 1992. GPS meteorology: remote sensing of atmospheric water vapor using the global positioning system. *J. Geophys. Res. Atmos.* 97 (D14), 15787–15801.
- Biggs, J., Wright, T., Lu, Z., Parsons, B., 2007. Multi-interferogram method for measuring interseismic deformation: Denali Fault, Alaska. *Geophys. J. Int.* 170 (3), 1165–1179.
- Blewitt, G., Hammond, W.C., Kreemer, C.J.E., 2018. Harnessing the GPS data explosion for interdisciplinary science. *Eos* 99 (10.1029), 485.
- Cao, Y., Li, Z., Wei, J., Hu, J., Duan, M., Feng, G., 2017. Stochastic modeling for time series InSAR: with emphasis on atmospheric effects. *J. Geod.* 92 (2), 185–204.
- Crosetto, M., Tscherning, C.C., Crippa, B., Castillo, M., 2002. Subsidence monitoring using SAR interferometry: reduction of the atmospheric effects using stochastic filtering. *Geophys. Res. Lett.* 29 (9), 261–264.
- Deng, Y., Hu, C., Tian, W., Zhao, Z., 2022. A grid partition method for atmospheric phase compensation in GB-SAR. *IEEE Trans. Geosci. Remote Sens.* 60, 1–13.
- Ding, X.L., Li, Z.W., Zhu, J.J., Feng, G.C., Long, J.P., 2008. Atmospheric effects on InSAR measurements and their mitigation. *Sensors (Basel)* 8 (9), 5426–5448.
- Doin, M.P., Lasserre, C., Peltzer, G., Cavalié, O., Doubre, C., 2009. Corrections of stratified tropospheric delays in SAR interferometry: validation with global atmospheric models. *J. Appl. Geophys.* 69 (1), 35–50.
- Falabella, F., Pepe, A., 2022. On the phase non-closure of multi-look SAR interferogram triplets. *IEEE Trans. Geosci. Remote Sens.* 1.
- Falabella, F., Perrone, A., Stabile, T.A., Pepe, A., 2022. Atmospheric phase screen compensation on wrapped ground-based SAR interferograms. *IEEE Trans. Geosci. Remote Sens.* 60, 1–15.
- Ferretti, A., Prati, C., Rocca, F., 2001. Permanent scatterers in SAR interferometry. *IEEE Trans. Geosci. Remote Sens.* 39 (1), 8–20.
- Fong, D.C.-L., Saunders, M., 2011. LSMR: an iterative algorithm for sparse least-squares problems. *SIAM J. Sci. Comput.* 33 (5), 2950–2971.
- Hanssen, R.F., 2001. Radar Interferometry: Data Interpretation and Error Analysis, Earth and Environmental Science Remote Sensing and Digital Image Processing, 2. In: Kluwer Academic Publishers, Dordrecht, The Netherlands, XVIII, p. 308.
- Hidayati, S., Sulaeman, C., 2013. Magma supply system at Batur volcano inferred from volcano-tectonic earthquakes and their focal mechanism. *Indonesian J. Geosci.* 8 (2), 97–105.
- Hooper, A., Segall, P., Zebker, H., 2007. Persistent scatterer interferometric synthetic aperture radar for crustal deformation analysis, with application to Volcán Alcedo, Galápagos. *J. Geophys. Res.* 112 (B7), B07407.
- Iglesias, R., Fabregas, X., Aguasca, A., Mallorqui, J.J., Lopez-Martinez, C., Gili, J.A., Corominas, J., 2014. Atmospheric phase screen compensation in ground-based SAR with a multiple-regression model over mountainous regions. *IEEE Trans. Geosci. Remote Sens.* 52 (5), 2436–2449.
- Jolivet, R., Agram, P.S., Lin, N.Y., Simons, M., Doin, M.-P., Peltzer, G., Li, Z., 2014. Improving InSAR geodesy using global atmospheric models. *J. Geophys. Res. Solid Earth* 119 (3), 2324–2341.
- Kumar, T.K., 1975. Multicollinearity in regression analysis. *Rev. Econ. Stat.* 57 (3), 365–366.
- Li, Z., Muller, J.-P., Cross, P., 2005. Interferometric synthetic aperture radar (InSAR) atmospheric correction: GPS, moderate resolution imaging spectroradiometer (MODIS), and InSAR integration. *J. Geophys. Res.* 110 (B3), B03410.
- Liang, H., Zhang, L., Ding, X., Lu, Z., Li, X., 2019. Toward mitigating stratified tropospheric delays in multitemporal InSAR: a quadtree aided joint model. *IEEE Trans. Geosci. Remote Sens.* 57 (1), 291–303.
- Liang, H., Zhang, L., Ding, X., Lu, Z., Li, X., Hu, J., Wu, S., 2021. Suppression of coherence matrix bias for phase linking and ambiguity detection in MTInSAR. *IEEE Trans. Geosci. Remote Sens.* 59 (2), 1263–1274.
- Lu, Z., Dzurisin, D., 2014. InSAR Imaging of Aleutian Volcanoes: Monitoring a Volcanic Arc from Space. *Geophysical Sciences*. Springer-Verlag Berlin Heidelberg.
- Maghsoudi, Y., Hooper, A.J., Wright, T.J., Lazecky, M., Ansari, H., 2022. Characterizing and correcting phase biases in short-term, multilooked interferograms. *Remote Sens. Environ.* 275, 113022.
- Markowski, P., Richardson, Y., 2011. Mesoscale Meteorology in Midlatitudes, 2. John Wiley & Sons.
- Massonnet, D., Rossi, M., Carmona, C., Adragna, F., Peltzer, G., Feigl, K., Rabaute, T., 1993. The displacement field of the Landers earthquake mapped by radar interferometry. *Nature* 364 (6433), 138–142.
- Mogi, K., 1958. Relations between the eruptions of various volcanoes and the deformations of the ground surfaces around them. *Bull. Earthquake Res. Inst.* 36, 99–134.
- Molan, Y.E., Lu, Z., Kim, J., 2020. Influence of the statistical properties of phase and intensity on closure phase. *IEEE Trans. Geosci. Remote Sens.* 1–9.
- Murray, K.D., Lohman, R.B., Bekaert, D.P.S., 2020. Cluster-based empirical tropospheric corrections applied to InSAR time series analysis. *IEEE Trans. Geosci. Remote Sens.* 1–9.
- Onn, F., Zebker, H.A., 2006. Correction for interferometric synthetic aperture radar atmospheric phase artifacts using time series of zenith wet delay observations from a GPS network. *J. Geophys. Res.* 111 (B9), B09102.
- Pipia, L., Fabregas, X., Aguasca, A., Lopez-Martinez, C., 2008. Atmospheric artifact compensation in ground-based DInSAR applications. *IEEE Geosci. Remote Sens. Lett.* 5 (1), 88–92.
- Wegmuller, U., Walter, D., Spreckels, V., Werner, C.L., 2010. Nonuniform ground motion monitoring with TerraSAR-X persistent scatterer interferometry. *IEEE Trans. Geosci. Remote Sens.* 48 (2), 895–904.
- Werner, C., Wegmuller, U., Strozzi, T., Wiesmann, A., 2003. Interferometric point target analysis for deformation mapping. *IGARSS 2003*. In: 2003 IEEE International Geoscience and Remote Sensing Symposium. Proceedings (IEEE Cat. No.03CH37477), vol.7, pp. 4362–4364.
- Wu, S., Yang, Z., Ding, X., Zhang, B., Zhang, L., Lu, Z., 2020. Two decades of settlement of Hong Kong international airport measured with multi-temporal InSAR. *Remote Sens. Environ.* 248, 111976.
- Yu, C., Li, Z., Penna, N.T., Crippa, P., 2018. Generic atmospheric correction model for interferometric synthetic aperture radar observations. *J. Geophys. Res. Solid Earth* 123 (10), 9202–9222.
- Zebker, H.A., Rosen, P.A., Hensley, S., 1997. Atmospheric effects in interferometric synthetic aperture radar surface deformation and topographic maps. *J. Geophys. Res. Solid Earth* 102 (B4), 7547–7563.
- Zhang, L., Ding, X., Lu, Z., Jung, H.-S., Hu, J., Feng, G., 2014. A novel multitemporal InSAR model for joint estimation of deformation rates and orbital errors. *IEEE Trans. Geosci. Remote Sens.* 52 (6), 3529–3540.
- Zhang, L., Lu, Z., Ding, X., Jung, H.-S., Feng, G., Lee, C.-W., 2012. Mapping ground surface deformation using temporarily coherent point SAR interferometry: application to Los Angeles Basin. *Remote Sens. Environ.* 117, 429–439.
- Zheng, Y., Fattahi, H., Agram, P., Simons, M., Rosen, P., 2022. On closure phase and systematic bias in multilooked SAR interferometry. *IEEE Trans. Geosci. Remote Sens.* 60, 1–11.